

Ethane precipitation occurs essentially in large regions poleward of $\pm 70^\circ$, with ~ 0.2 mm per Titan year in polar regions and a few micrometers per year elsewhere. The methane cycle is a balance between the surface evaporation and precipitation. Methane evaporates between the tropics (in the $\pm 30^\circ$ range) and precipitates near the poles. In tropical regions, most of the methane clouds evaporate before reaching the ground, except for the largest ones. At latitudes of $\pm 70^\circ$, methane precipitation does not exceed 1 cm per year, but poleward of $\pm 70^\circ$ it can reach 1 m per year. The global cycle then drives methane from equatorial and tropical to polar regions. Methane is probably not stable in tropical regions on geological time scales, and because the Huygens landing site was humid and marked by river channels, this indicates that a source of methane is still active on Titan (28). Global average values of precipitation rates found here are consistent with previous work (14, 17).

The methane cycle on Titan has some similarities with water cycles on Earth and on Mars. As with water on Earth and Mars, the methane source on Titan is at the surface. The major cloud pattern on these planets essentially appears in ascending branches of the circulation: (i) The Hadley cell system produces a cloud belt in the intertropical convergence zone on Earth and on Mars and also produces the frequent clouds at 40° in the summer hemisphere on Titan. (ii) The poleward ascending motions beyond the Hadley cell, developed as baroclinic waves on Earth and on Mars and as slantwise convection in our two-dimensional model of Titan, produces clouds because water or methane-rich air is transported toward cold regions. This mechanism produces the south polar cloud. Baroclinic waves are believed not

to be produced on Titan (17). In these three atmospheres, clouds are generally good tracers of the circulation and can reveal some of its important features.

Gravitational tides caused by Saturn are known to disturb the large-scale circulation (29). This effect is specific to Titan and could explain the longitudinal large-scale distribution of the clouds (11) by triggering nucleation at preferential longitudes. Surface heterogeneities (albedo contrasts and topography) and waves may also play a role in circulation and in cloud meteorology. These questions must be addressed further, in the frame of a three-dimensional model.

Some cloud properties may be defined, in reality, at scales smaller than the model grid [e.g., cloud overshoots, subscale inhomogeneities as observed by (9)]. Interaction between clouds and haze in our model may also lead to removal of aerosols more efficiently than observed in reality (27). Clouds in our circulation model are necessarily simplified relative to the real clouds. However, the main cloud features predicted in this work find a counterpart in reality. The correct behavior of our model allows us to analyze the formation mechanism associated with each type of observed cloud and offers a new insight into cloud physics on Titan.

References and Notes

1. R. E. Samuelson, L. A. Mayo, M. A. Knuckles, R. J. Khanna, *Planet. Space Sci.* **45**, 941 (1997).
2. C. A. Griffith, T. Owen, G. A. Miller, T. Geballe, *Nature* **395**, 575 (1998).
3. C. A. Griffith, J. L. Hall, T. R. Geballe, *Science* **290**, 509 (2000).
4. M. E. Brown, A. H. Bouchez, C. A. Griffith, *Nature* **420**, 795 (2002).
5. S. G. Gibbard *et al.*, *Icarus* **169**, 429 (2004).
6. C. C. Porco *et al.*, *Nature* **434**, 159 (2005).

7. H. G. Roe, I. De Pater, B. A. Macintosh, C. P. McKay, *Astron. J.* **591**, 1399 (2002).
8. A. H. Bouchez, M. E. Brown, *Astron. J.* **618**, L53 (2005).
9. C. A. Griffith *et al.*, *Science* **310**, 474 (2005).
10. H. G. Roe, A. H. Bouchez, C. A. Trujillo, E. L. Schaller, M. E. Brown, *Astron. J.* **618**, L49 (2005).
11. H. G. Roe, M. E. Brown, E. L. Schaller, A. H. Bouchez, C. A. Trujillo, *Science* **310**, 477 (2005).
12. R. Courtin, D. Gautier, C. P. McKay, *Icarus* **114**, 144 (1995).
13. R. E. Samuelson, L. A. Mayo, *Planet. Space Sci.* **45**, 949 (1997).
14. E. L. Barth, O. B. Toon, *Icarus* **162**, 94 (2004).
15. R. D. Lorenz, *Planet. Space Sci.* **41**, 647 (1993).
16. E. L. Barth, O. B. Toon, *Geophys. Res. Lett.* **31**, L17507 (2005).
17. T. Tokano, F. M. Neubauer, M. Laube, C. P. McKay, *Icarus* **153**, 130 (2001).
18. F. Hourdin *et al.*, *Icarus* **117**, 358 (1995).
19. P. Rannou, F. Hourdin, C. P. McKay, *Nature* **418**, 853 (2002).
20. P. Rannou, F. Hourdin, C. P. McKay, D. Luz, *Icarus* **170**, 443 (2004).
21. See supporting material on Science Online.
22. E. F. Young, P. Rannou, C. P. McKay, C. A. Griffith, K. Noll, *Astron. J.* **123**, 3473 (2002).
23. S. Lebonnois, D. Toubanc, F. Hourdin, P. Rannou, *Icarus* **152**, 384 (2001).
24. F. Hourdin, S. Lebonnois, D. Luz, P. Rannou, *J. Geophys. Res.* **109**, E10005 (2004).
25. L. A. Mayo, R. E. Samuelson, *Icarus* **176**, 316 (2005).
26. H. B. Niemann *et al.*, *Nature* **438**, 779 (2005).
27. M. Tomasko *et al.*, *Nature* **438**, 765 (2005).
28. C. Sotin *et al.*, *Nature* **435**, 786 (2005).
29. T. Tokano, F. M. Neubauer, *Icarus* **158**, 499 (2002).
30. R. E. Samuelson, N. R. Nath, A. Borysov, *Planet. Space Sci.* **45**, 959 (1997).
31. Supported by the Programme National de Planétologie du CNRS. This work was performed while F.M. held a tenure from the National Research Council associateship program.

Supporting Online Material

www.sciencemag.org/cgi/content/full/311/5758/201/DC1
Materials and Methods
Figs. S1 and S2
Table S1
References

4 August 2005; accepted 9 November 2005
10.1126/science.1118424

Majority Logic Gate for Magnetic Quantum-Dot Cellular Automata

A. Imre,^{1*} G. Csaba,² L. Ji,¹ A. Orlov,¹ G. H. Bernstein,¹ W. Porod¹

We describe the operation of, and demonstrate logic functionality in, networks of physically coupled, nanometer-scale magnets designed for digital computation in magnetic quantum-dot cellular automata (MQCA) systems. MQCA offer low power dissipation and high integration density of functional elements and operate at room temperature. The basic MQCA logic gate, that is, the three-input majority logic gate, is demonstrated.

In magnetic devices, information is encoded in the magnetization state of ferromagnetic materials. Although commonly used for data-storage applications, there are relatively few attempts to exploit magnetic phenomena for logic functionality (1–5). One of the possible architectures suitable for logic using nanomagnets is the quantum-dot cellular automata (QCA) signal-processing approach (6). QCA are built from simple, (nominally) identical,

bistable units that are locally connected to each other solely by electromagnetic forces; consequently, the signal-processing function is defined by the physical placement of the building blocks that constitute the computing architecture (7–9). Recently, Cowburn and Welland (2) described the realization of magnetic QCA (MQCA) operation in chains of 110-nm-diameter disk-shaped magnetic particles that manifest collective behavior. In this system,

the preferred magnetization direction of the disks (the representation of binary information), as well as the magnetization reversal process (the information propagation), is primarily determined by coupling-induced magnetic anisotropy in the chains. Our approach to MQCA is similar in spirit, but we use an additional shape-induced anisotropy component to separate the directions for magnetic information representation and information propagation in the array (5).

The QCA concept can be realized in different physical systems. It was originally proposed to use electrostatically coupled arrays of quantum dots and Coulomb-blockade phenomena to perform binary operations (6). The

¹Center for Nano Science and Technology, Department of Electrical Engineering, University of Notre Dame, Notre Dame, IN 46556, USA. ²Institute for Nanoelectronics, Technical University of Munich, Arcisstrasse 21, D-80333 Munich, Germany.

*To whom correspondence should be addressed. E-mail: aimre@nd.edu

first functional electrostatic QCA (EQCA) cell was experimentally demonstrated (10) in 1997, followed by the logic gate (11) and the shift register (12). Micrometer-sized metal (Al) dots separated by thin (a few nm) oxide tunnel barriers were used in these experiments, which were performed at subkelvin temperatures owing to small charging energies ($\sim k_B \times 1$ K, where k_B is the Boltzmann constant) achievable with this fabrication technique (13). Room-temperature EQCA can be achieved only for the size of a cell reduced to molecular scale (14, 15), the technology for which has not yet been demonstrated.

As an advantage compared to the above-mentioned electrostatic devices, logic gates featuring single-domain magnets on the size scale of 10 to 100 nm (above the superparamagnetic limit, but within the single-domain limit) are expected to operate at room temperature because of their relatively large magnetic energies (5, 16). Consider an elongated single-domain magnet similar in shape and magnetic state to the larger magnets in the one-domain state shown in Fig. 1. Being of submicrometer size, elongated single-domain magnets are strongly bistable, because their remanent magnetization (magnetization at zero external field) always points along their long axis owing to shape-induced magnetic anisotropy. Even though a magnetizing force can temporarily rotate the magnetization away from the long axis, the magnet relaxes to either of the two remanent states when the force is removed. The process of temporarily magnetizing perpendicular to the long axis can be pictured as the magnetizing force pulling down and then releasing the energy barrier between the remanent ground states.

For the one-domain state, unlike the two-domain or vortex configurations (also shown in Fig. 1), the magnetic flux lines close outside of the magnets, creating strong magnetic stray fields that can be used to couple elements in close proximity through dipole-dipole interactions. The resulting magnetization pattern for an array of nanomagnets depends on their physical arrangement. For example, arranging several of these magnets to be colinear along their long axes results in a line of magnets favoring their magnetization to point in the same direction, i.e., the ferromagnetically ordered state. Placing them side-by-side and in parallel results in a line that favors antiparallel alignment of the magnetic dipoles, i.e., the antiferromagnetically ordered state. In MQCA, these coupling-induced ordering phenomena are used to drive the computation.

Figure 2 shows a line of antiferromagnetically coupled (AFC) nanomagnets elongated in the “vertical” direction (the y direction). Also shown on the right-hand side of the line is a “horizontal” nanomagnet (the x direction), which can be used as an input to set the state of the linear array. In the absence of the input

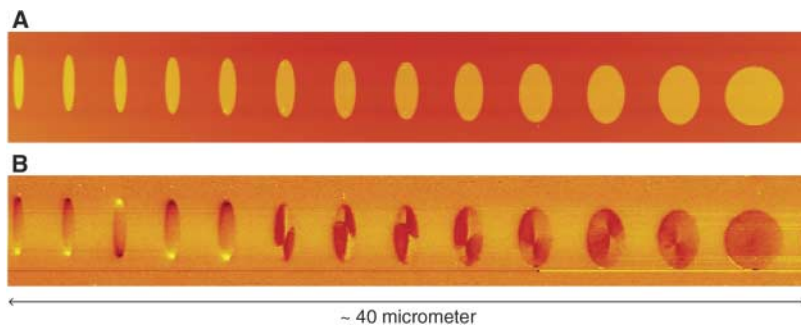
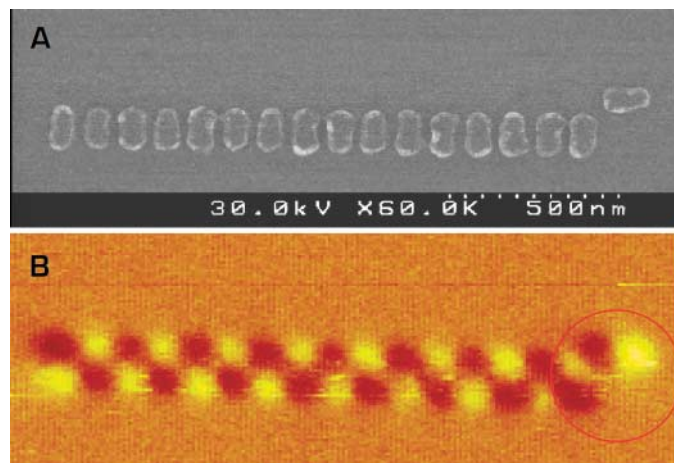


Fig. 1. Magnetic states of patterned ferromagnetic elements. (A) Topographic atomic force microscope (AFM) image of thin-film, polycrystalline NiFe magnetic elements in a row, made by electron-beam lithography and lift-off. While one axis of the oval elements is kept the same, the aspect ratio of the axes is varied between 7.5 (on the left side) to 1 (on the right side). (B) MFM image of remanent magnetization. Strong contrast in the MFM images of one-domain magnets represents the location of magnetic poles. This image reveals one-domain, two-domain, and vortex configurations, depending upon the size and shape (aspect ratio) of the elements.

Fig. 2. Antiferromagnetic ordering in a line of nanomagnets. (A) Scanning electron microscope (SEM) image of a chain of 16 coupled nanomagnets of size 70 nm by 135 nm and 30-nm permalloy thickness. The separation between the vertically elongated magnets is 25 nm. The antiferromagnetic ordering along the chain is controlled by an additional, horizontally oriented elongated driver magnet. (B) MFM image of the same chain shows alternating magnetization of the magnets as set by the state of the horizontal driver magnet (circled).



magnet, the ground state of the AFC line could be one of two possible complementary, alternating dipole configurations (either up-down-up-down...etc. or down-up-down-up...etc.). Setting the state of the input magnet by an external field in the x direction breaks this symmetry and favors one of the two possible complementary states of the line. This input magnetic field, if designed properly, can also be used to act as an adiabatic clocking field (hereafter referred to as the clock-field) to facilitate the switching of the line from some arbitrary state to the AFC ground state. The effect of such a horizontal field on the vertical dots is to add an x component of magnetization to the preferred y direction. For sufficiently strong clock-fields (typically several hundred Oe), the magnetization vectors of all nanomagnets in the line can be forced to point in the x direction, but this state will persist only so long as the clock-field is maintained, and the nanomagnets will return to their preferred state with magnetization in the y direction upon removal of this field. The crucial

point here is that this switching behavior from magnetization in the x direction to either up or down in the y direction is strongly influenced by any additional fields, such as coupling fields from either the neighbors or the input magnet. The effect of the clock-field in the x direction is to place the line of coupled magnets into an intermediate state, and the magnetic fringe fields from inputs and neighbors then determine which ground-state configuration the array assumes after removal of the clock-field. We have both studied this switching behavior through extensive micromagnetic simulations (16) and observed it experimentally (Fig. 2B).

We introduce in Fig. 3 a gated AFC line that performs majority logic. The nanomagnets are arranged in two intersecting lines, such that the dipole coupling of the nanomagnets produces ferromagnetic ordering along the vertical line and antiferromagnetic ordering along the horizontal line. This structure is similar to that proposed in (17) [and also studied in (18)], except that we consider the

Fig. 3. Majority gates designed for testing all input combinations of the majority-logic operation. The arrows drawn superimposed on the SEM images illustrate the resulting magnetization direction due to a horizontally applied external clock-field. The magnetic state of the AFC inputs has the opposite effective votes on the central magnet as compared with the FC inputs, so AFC and FC inputs are assigned the same logical value for opposite magnetizations. The bit value “0” is assigned to magnetization direction down along the vertical axis of FC input magnets and the central magnet, and value “1” is assigned to magnetization up. The AFC input is defined oppositely.

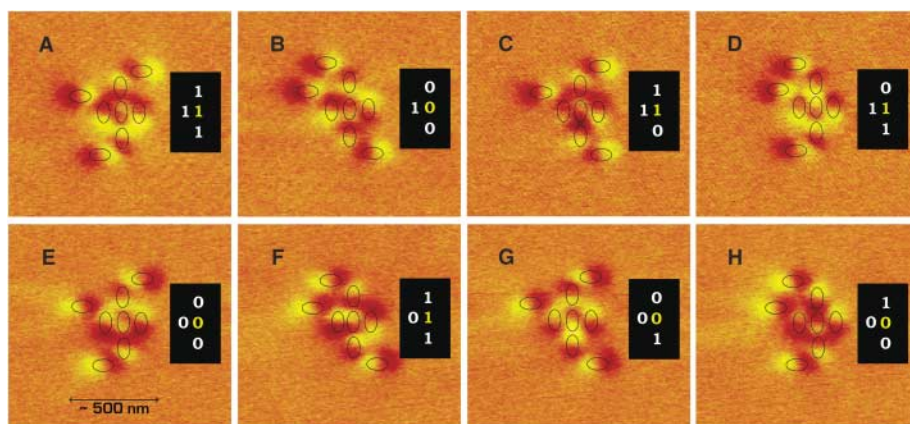
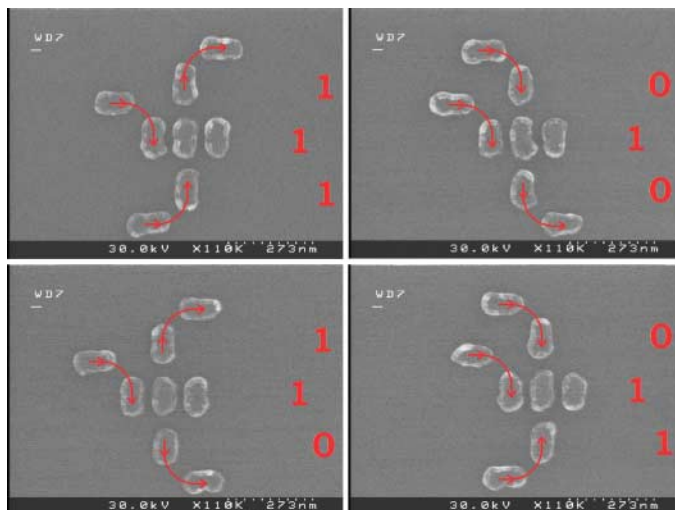


Fig. 4. MFM images of functioning majority gates. The location of the magnets is drawn superimposed on the MFM data. (A to D) Clock-field applied horizontally to the right and (E to H) to the left. Bit values assigned to the magnetization directions can be determined by the MFM contrast. Bit values shown in (I) are for FC inputs and central magnet. (AFC inputs are designated with the inverse logical values.) The black insets show alignment of magnetic dipoles, accounting for antiferromagnetic and ferromagnetic coupling, and demonstrate correct MQCA majority logic gate functionality.

output of the gate to be in the AFC line instead of the FC line. Consider the simplest arrangement of five nanomagnets, i.e., a central nanomagnet surrounded by four others. Three of the neighbors can be used as inputs driven by additional driver nanomagnets oriented in the x direction, along the clock-field. The fourth neighbor, to the right of the central magnet in Fig. 3, is the output. Our gate is constructed so that the ferromagnetic and antiferromagnetic coupling to the central dot have the same strength, and therefore it switches to the state to which the majority of inputs force it. By varying the positions of the driver nanomagnets, all eight input logic combinations can be tested, as suggested in the figure.

Simulations (19) of the magnetic states of the majority gates after applying a horizontal

clock-field show that as the clock-field falls, switching inside the gate begins at the input magnets and ends at the output magnet. Figure 4 demonstrates final states after two experiments in which a clock-field of 500 Oe with ~ 30 -s rise and fall times (20) was applied in opposite directions. Inputs (000), (001), (010), and (011) were written by the driver magnets when the clock-field was oriented to the left and (100), (101), (110), and (111) when oriented to the right. The function of the majority gate is given in the included truth table (Table 1) in terms of the central magnet. The magnetic force microscopy (MFM) data (21) in Fig. 4 show correct alignment of all magnetic dipoles of the gates.

Our investigations demonstrate that correct operation of the majority-gate structure (as

Table 1. Summary of logic states in the majority gate for all input combinations (truth table). The logic state of the central nanomagnet is determined by the logical majority vote of its three input neighbors, of which the ferromagnetically coupled neighbors vote directly and the antiferromagnetically coupled neighbor votes inversely to its magnetic state. The logic state of the central magnet is written inverted to the output magnet by antiferromagnetic coupling. If programmed by the first-input bit value, a majority gate can function as a two-input NAND gate (upper four rows of the table) or as a two-input NOR gate (lower four rows of the table).

Logic state of input magnets	Logic state of central magnet	Logic state of output magnet
000	0	1
001	0	1
010	0	1
011	1	0
100	0	1
101	1	0
110	1	0
111	1	0

defined by every magnet being consistent with the applied field) was found in about 25% of the set of fabricated gates when the applied clock-field was aligned to the horizontal with approximately $\pm 1^\circ$ of accuracy. It is important to note that the probability of all eight nanomagnets assuming the correct orientation is less than 0.4%. We observed a much larger fraction of fully correct logic gates, which demonstrates that our results cannot be random events. We believe that fabrication variations are responsible for yields of less than 100% (22). The run-to-run reliability was about 50%, indicating that between runs, about half of the working gates were in common. We believe that this was mostly due to clock-field misalignment between runs.

The three-input majority gate discussed above can be viewed as a programmable two-input NAND or NOR gate, depending on the state of any one of the three input magnets and accounting for inversion at the output magnet. Therefore, any Boolean logic function can be built by a network of majority gates. The inputs used in this work are set by the external clock-field and cannot be programmed independently; different combinations of the input values are realized by different physical arrangements of driver magnets. Nevertheless, the intersection of the horizontal and vertical wires, which is common to all structures, can correctly perform majority-logic functionality. We are currently developing inputs that can be controlled independently.

The minimum time necessary for magnetic switching is limited by magnetization precession in the nanomagnets and is on the order of 100 ps (23). The adiabatic pumping scheme

further increases the clock-cycle time in MQCA devices by one or two orders of magnitude to eliminate precession from the switching process and to ensure predictable operation. Our simulations show that the majority gate reported here has an inherent operating speed of 100 MHz and dissipation below 1 eV per switching event. As a worst-case estimate of the power dissipation in an MQCA system, at these speeds, and assuming that all nanomagnets switch in each clock cycle, 10^{10} gates would dissipate ~ 0.1 W.

We performed Monte Carlo simulations in the single-domain approximation to investigate whether the realization of larger-scale systems is feasible (24). Variations in nanomagnet shape and edge roughness were taken into account in the distribution of the coupling fields at which switching occurs, i.e., switching fields (distribution of the demagnetization tensor elements), and thermal fluctuations were modeled by adding a stochastic field to the coupling field. We found that for our structures, the impact of switching-field variations is far more important than the effect of thermal fluctuations. Strongly coupled dots (<100 -nm dot separation) fabricated by high-quality lithography (with switching-field variations less than 10%) exhibit magnetic ordering over 10 to 20 magnets. This result agrees well with our previous experiments (25, 26) for samples fabricated by electron-beam lithography and lift-off (supporting online text). Even with better fabrication technology, the number of nanomagnets that can be clocked together is limited. Therefore, a larger-scale device would have to operate by means of local clocking of subarrays that realize a few gates only. The small number of magnets switching at the same time ensures that error levels can be kept acceptably small. This concept has been developed for EQCA (27). The most suitable architecture for adiabatically clocked MQCA devices appears to be a pipelined structure. Because of the sequential arrangement of logic gates, there will inevitably be pipeline latency; however, new data can be fed into the pipeline at each clock cycle. Clocking zones can be defined by locally applied clock-fields. Pipelined architectures are desirable in their own right owing to their highly parallelized computing environment.

Integration of MQCA elements with electronic circuitry is possible in a manner similar to that for magnetic random access memory (MRAM) elements (28). Furthermore, integration of MQCA arrays into MRAM cells is also feasible, thus allowing the possibility of "intelligent memory" whereby the magnetic layer of an MRAM cell could not only store a single bit of information, but could also perform basic logical processing. This may provide an opportunity to increase the functionality and integration density of an MRAM device.

In summary, MQCA information propagation and negation have been demonstrated previously (2, 25, 26), and our present work indicates that logic functions can also be realized in properly structured arrays of physically coupled nanomagnets. The technology for fabricating such nanometer-scale magnets is currently under development by the hard disk drive industry (29). Whereas the latter work focuses entirely on data-storage applications, and physical coupling between individual bits is undesirable, our work points out the possibility of also realizing logic functionality in such systems and indicates the potential of all-magnetic information-processing systems that incorporate both memory and logic.

References and Notes

1. A. Ney, C. Pampuch, R. Koch, K. H. Ploog, *Nature* **425**, 485 (2003).
2. R. P. Cowburn, M. E. Welland, *Science* **287**, 1466 (2000).
3. D. A. Allwood *et al.*, *Science* **296**, 2003 (2002).
4. D. A. Allwood *et al.*, *Science* **309**, 1688 (2005).
5. G. Csaba, A. Imre, G. H. Bernstein, W. Porod, V. Metlushko, *IEEE Trans. Nanotechnol.* **1**, 209 (2002).
6. C. S. Lent, P. D. Tougaw, W. Porod, G. H. Bernstein, *Nanotechnology* **4**, 49 (1993).
7. A. I. Csurgay, W. Porod, C. S. Lent, *IEEE Trans. Circ. Syst. I* **47**, 1212 (2000).
8. G. Csaba, A. I. Csurgay, W. Porod, *Int. J. Circ. Theory Appl.* **29**, 73 (2001).
9. G. Csaba, W. Porod, A. I. Csurgay, *Int. J. Circ. Theory Appl.* **31**, 67 (2003).
10. A. O. Orlov, I. Amlani, G. H. Bernstein, C. S. Lent, G. L. Snider, *Science* **277**, 928 (1997).
11. I. Amlani *et al.*, *Science* **284**, 289 (1999).
12. R. K. Kummamuru *et al.*, *IEEE Trans. Electron Devices* **50**, 1906 (2003).
13. A. O. Orlov *et al.*, *Mesoscopic Tunneling Devices*, H. Nakashima, Ed. (Research Signpost, Trivandrum, Kerala, India, 2004), p. 125.
14. G. L. Snider *et al.*, *J. Appl. Phys.* **85**, 4283 (1999).
15. C. S. Lent, *Science* **288**, 1597 (2000).

16. G. Csaba, W. Porod, *J. Comput. Electron.* **1**, 87 (2002).
17. M. C. B. Parish, M. Forshaw, *Appl. Phys. Lett.* **83**, 2046 (2003).
18. S. A. Haque, M. Yamamoto, R. Nakatani, Y. Endo, *J. Magn. Mater.* **282**, 380 (2004).
19. The micromagnetic simulations were performed using the Object Oriented Micromagnetic Framework (M. J. Donahue, D. G. Porter, OOMMF User's Guide, Version 1.0 Interagency Report NISTIR 6376, <http://math.nist.gov/oommf/>) of the National Institute of Standards and Technology.
20. The magnetizing process, i.e., the application of the clock-field, was performed in the homogeneous field of an electromagnet capable of a maximum 7000 Oe. Owing to limitations imposed by the ramping rate of the generated field, the frequency of the clock-field was about 0.01 Hz in our experiments.
21. Magnetic force microscopy images were taken in a Digital Instruments Nanoscope IV with standard magnetic probes.
22. Antiferromagnetic ordering was investigated in a large set of AFC lines designed to be identical. In a small percentage of results, we have found the ordering to fail even in the simplest, two-magnet systems. The identified faulty pairs performed highly repeatably, which indicates that the errors are related to fabrication variations (30).
23. Th. Gerrits, H. A. M. van den Berg, J. Hohlfeld, L. Bar, Th. Rasing, *Nature* **418**, 509 (2002).
24. G. Csaba, thesis, University of Notre Dame, IN (2003).
25. A. Imre, G. Csaba, G. H. Bernstein, W. Porod, V. Metlushko, *Proc. IEEE Nanotechnol.* **2**, 20 (2003).
26. A. Imre, G. Csaba, G. H. Bernstein, W. Porod, V. Metlushko, *Superlatt. Microstruct.* **34**, 513 (2003).
27. J. Timler, C. S. Lent, *J. Appl. Phys.* **91**, 823 (2002).
28. C. A. Ross, *Annu. Rev. Mater. Res.* **31**, 203 (2001).
29. J. M. Slaughter *et al.*, *J. Supercon.* **15**, 19 (2002).
30. G. H. Bernstein *et al.*, *Microelectr. J.* **36**, 619 (2005).
31. This work was supported in part by grants from the Office of Naval Research, the W. M. Keck Foundation, and the National Science Foundation.

Supporting Online Material

www.sciencemag.org/cgi/content/full/311/5758/205/DC1
SOM Text
References

23 September 2005; accepted 1 December 2005
10.1126/science.1120506

A Stretchable Form of Single-Crystal Silicon for High-Performance Electronics on Rubber Substrates

Dahl-Young Khang,^{1,3,4} Hanqing Jiang,² Young Huang,^{2*} John A. Rogers^{1,2,3,4*}

We have produced a stretchable form of silicon that consists of submicrometer single-crystal elements structured into shapes with microscale, periodic, wavelike geometries. When supported by an elastomeric substrate, this "wavy" silicon can be reversibly stretched and compressed to large levels of strain without damaging the silicon. The amplitudes and periods of the waves change to accommodate these deformations, thereby avoiding substantial strains in the silicon itself. Dielectrics, patterns of dopants, electrodes, and other elements directly integrated with the silicon yield fully formed, high-performance "wavy" metal oxide semiconductor field-effect transistors, p-n diodes, and other devices for electronic circuits that can be stretched or compressed to similarly large levels of strain.

Progress in electronics is driven mainly by efforts to increase circuit operating speeds and integration densities, to reduce the power consumption of circuits, and, for display systems, to enable large area co-

verage. A more recent direction seeks to develop methods and materials that enable high-performance circuits to be formed on unconventional substrates with unusual form factors (1, 2), such as flexible plastic substrates for